



## Modeling the effects of a solid barrier on pollutant dispersion under various atmospheric stability conditions

Jonathan T. Steffens<sup>a</sup>, David K. Heist<sup>b</sup>, Steven G. Perry<sup>b</sup>, K. Max Zhang<sup>a,\*</sup>

<sup>a</sup>Sibley School of Mechanical and Aerospace Engineering, Cornell University, Ithaca, NY 14853, United States

<sup>b</sup>Atmospheric Modeling Division, National Exposure Research Laboratory, MD 81-U.S. Environmental Protection Agency, Research Triangle Park, NC 27709, United States

### HIGHLIGHTS

- ▶ The LES and  $k-\epsilon$  RANS models are employed to model how a solid barrier affects dispersion.
- ▶ Modeling results are evaluated against the NRTS08 dataset.
- ▶ LES performs consistently well under all atmospheric conditions.
- ▶ The  $k-\epsilon$  RANS model cannot fully capture the edge and recirculation.

### ARTICLE INFO

#### Article history:

Received 11 June 2012

Received in revised form

19 November 2012

Accepted 20 November 2012

#### Keywords:

Pollutant dispersion

Flow recirculation

CFD

Modeling

### ABSTRACT

There is a growing need for developing mitigation strategies for near-road air pollution. Roadway design is being considered as one of the potential options. Particularly, it has been suggested that sound barriers, erected to reduce noise, may prove effective at decreasing pollutant concentrations. However, there is still a lack of mechanistic understanding of how solid barriers affect pollutant transport, especially under a variety of meteorological conditions. In this study, we utilized the Comprehensive Turbulent Aerosol Dynamics and Gas Chemistry (CTAG) model to simulate the spatial gradients of SF<sub>6</sub> concentrations behind a solid barrier under a variety of atmospheric stability conditions collected during the Near Road Tracer Study (NRTS08). We employed two different CFD models, RANS and LES. A recirculation zone, characterized by strong mixing, forms in the wake of a barrier. It is found that this region is important for accurately predicting pollutant dispersion, but is often insufficiently resolved by the less complex RANS model. The RANS model was found to perform adequately away from the leading edge of the barrier. The LES model, however, performs consistently well at all flow locations. Therefore, the LES model will make a significant improvement compared to the RANS model in regions of strong recirculating flow or edge effects. Our study suggests that advanced simulation tools can potentially provide a variety of numerical experiments that may prove useful for roadway design communities to intelligently design roadways, making effective use of roadside barriers.

© 2012 Elsevier Ltd. All rights reserved.

### 1. Introduction

Studies have shown that people who live, work, or go to school near roadways are at risk for a variety of health problems, including respiratory and cardiovascular problems, birth and developmental defects, and cancer, due to exposure to harmful traffic-related air pollutants (HEI, 2010). In addition to vehicle emissions control, there are potential opportunities for mitigating near-road air pollution in roadway design options that affect pollutant transport and dispersion such as road configurations and the presence of

roadside barriers (Bowker et al., 2007; Baldauf et al., 2008; Cahill, 2010). Designing or evaluating roadside barriers to maximize their benefits requires a mechanistic understanding on how barrier geometry location and traffic and meteorological conditions affect the fate and transport of traffic-related air pollutants. Recent wind tunnel experiments and field measurements (Heist et al., 2009; Finn et al., 2010) have begun to characterize the effects of roadside barriers. Additionally, much work has recently been done with experiment and simulation in urban street canyons (Chang and Meroney, 2003; Neophytou et al., 2011; Xie and Castro, 2009). However, significant knowledge gaps exist in terms of both our fundamental understanding and practical applications of using roadside barriers to mitigate near-road air pollution.

\* Corresponding author.

E-mail address: [kz33@cornell.edu](mailto:kz33@cornell.edu) (K.M. Zhang).

This paper continues our efforts in developing predictive tools in elucidating the effects of roadside barriers on near-road air quality. Our modeling framework is called the Comprehensive Turbulent Aerosol Dynamics and Gas Chemistry (CTAG) model. It is a computational fluid dynamics (CFD)-based environmental turbulent reacting flow model designed to simulate the transport and transformation of multiple air pollutants on and near roadways, taking into consideration roadway design including vehicle induced turbulence (VIT) created by vehicular traffic and roadway induced turbulence (RIT) created by the roadway design such as roadway configurations, roadside buildings and roadside barriers (Wang and Zhang, 2009, 2012; Wang et al., 2011; Tong et al., 2012). Previously, we created and evaluated a computational model within the CTAG framework to assess the impact of a roadside vegetation barrier (Steffens et al., 2012). Our sensitivity analysis suggests that fully capturing the flow field is critical to improving the prediction of particle size distributions. While some computational models have been applied to urban environments (Gowardhan et al., 2011; Hanna et al., 2002), relatively few modeling studies have specifically addressed the case of solid barriers, such as sound walls. Hagler et al. (2011) compared the simulation results from a Reynolds Averaged Navier–Stokes (RANS) model against the wind tunnel measurements conducted by Heist et al. (2009). However, only one stability condition was investigated in Heist et al. (2009). Modeling can provide insight into the behavior of air flow and pollutant transport in these areas.

In this paper, we apply two CFD models to investigate the effects of a solid barrier on downwind pollutant concentrations. The models we employ are the RANS model and the Large Eddy Simulation (LES) model. The RANS model requires a turbulence model to close the system and the LES model requires a subgrid model, as described in Section 2. There are a number of options for these models. Since the goal of this work is the comparison of RANS and LES in general, we have selected basic, commonly used models. We utilize the  $k$ - $\varepsilon$  turbulence model and the Smagorinsky–Lilly subgrid model for the RANS and LES models, respectively. The RANS model is often used due to its wide general applicability and fairly low computational cost. The LES model offers overall greater accuracy but at the cost of much higher computational times, due to finer meshing requirements and the requirement of an unsteady flow solver. There are three main objectives in our study: 1) to examine the capabilities of different CFD models in resolving the flow fields and pollutant transport behind a solid barrier by comparing model predictions with open field measurements under a variety of atmospheric stability conditions; 2) to quantify the accuracy of both a RANS and LES model in order to give guidelines for when a less complex model is appropriate and when a more complex model is needed; and 3) to deepen our understanding on the underlying physical mechanisms that contribute to pollutant transport across the solid barrier with the validated models. All three objectives will help to further improve the CTAG model in terms of simulating the effects of roadside barriers.

## 2. Model description

The CTAG model contains the functionality to fully resolve the flow field including turbulent reacting flows, aerosol dynamics and gas chemistry. More information about the model is found in Wang and Zhang (2009, 2012), Wang et al., (2011, 2013), and Tong et al., 2012. The CTAG model employs ANSYS Fluent commercial software package (ANSYS Inc., 2009) as the CFD flow solver. Flow simulations are often highly sensitive to the type of flow model employed. As such, this paper will investigate the effects of both a RANS model and a LES model on the flow field simulations. Both the RANS and LES flow models are derived from the Navier–Stokes

and Continuity equations and must include further models to fully close the system of equations. In this paper, the RANS model employs the  $k$ - $\varepsilon$  turbulent flow solver to compute the turbulence field and the LES model employs the Smagorinsky–Lilly subgrid model.

The RANS equations are derived by averaging the instantaneous velocities in the governing equations. Mass conservation is given by the equation:

$$\frac{\partial u_i}{\partial x_i} = 0 \quad (1)$$

and the Reynolds Averaged Navier–Stokes (RANS) equations can be written as:

$$\rho u_j \frac{\partial u_i}{\partial x_j} = -\frac{\partial P}{\partial x_i} + \mu \frac{\partial}{\partial x_j} \left( \frac{\partial u_i}{\partial x_j} + \frac{\partial u_j}{\partial x_i} \right) - \rho \frac{\partial \overline{u'_i u'_j}}{\partial x_j} + S_u \quad (2)$$

where  $\rho$  is the fluid density,  $u_i$  is the  $i$ th component of velocity,  $x_j$  is the direction vector,  $P$  is pressure,  $\mu$  is viscosity,  $\overline{u'_i u'_j}$  is the Reynolds Stress tensor and  $S_u$  is any additional source term.

This averaging creates a closed system except for the Reynolds Stress term that is introduced. Various methods for computing this property exist. Eddy viscosity models, such as the  $k$ - $\varepsilon$  model, relate the Reynolds Stresses to the mean flow by way of a turbulent eddy viscosity using the Boussinesq eddy viscosity assumption. The  $k$ - $\varepsilon$  model computes the eddy viscosity and closes the system by introducing transport equations for turbulent kinetic energy, TKE, and turbulent dissipation,  $\varepsilon$ , given by (Jones and Lauder, 1972):

$$u_j \frac{\partial k}{\partial x_j} = \frac{\partial}{\partial x_j} \left( \frac{\mu_t}{\rho \sigma_k} \frac{\partial k}{\partial x_j} \right) + P_k - \varepsilon + S_k \quad (3)$$

$$u_j \frac{\partial \varepsilon}{\partial x_j} = \frac{\partial}{\partial x_j} \left( \frac{\mu_t}{\rho \sigma_\varepsilon} \frac{\partial \varepsilon}{\partial x_j} \right) + C_1 \frac{\varepsilon}{k} P_k - C_2 \frac{\varepsilon^2}{k} + S_\varepsilon \quad (4)$$

where  $P_k$  is the production of turbulent kinetic energy and  $C_1$  and  $C_2$  are model constants. The model constants were selected based on the values given in Lauder and Sharma (1974) which have been found to be sufficiently accurate for a wide variety of turbulent flows.

The LES model is formulated based on the principal that important flow properties, such as momentum, mass, and energy, are transported primarily by the larger eddies in the flow. Additionally, large eddies are more dependent on the specific problem configuration, i.e. geometry and inlet conditions, while small eddies tend to behave more universally. As such, LES models explicitly resolves the large scale eddies found in turbulent flow by solving filtered Navier–Stokes equations. Smaller eddies, residing in the subgrid, are modeled. LES is much more computationally expensive than RANS models in part because the LES model requires an unsteady numerical scheme. Additionally, resolution of the turbulent eddies requires a finer grid than is necessary for a RANS model. In practice, LES schemes explicitly resolve the eddies that contain the majority of the flow energy, usually 80% or more (Pope, 2000). Further resolution of the turbulent eddies requires smaller grid size, which in turn requires a smaller time step, increasing the computational time by many factors. Thus, LES strikes a balance between the less accurate RANS models and fully resolving the flow, such as a Direct Numerical Simulation (DNS). The filtered forms of the continuity and Navier–Stokes equations given by:

$$\frac{\partial p}{\partial t} + \frac{\partial}{\partial x_j} (\rho \bar{u}_i) = 0 \quad (5)$$

$$\frac{\partial}{\partial t} (\rho \bar{u}_i) + \frac{\partial}{\partial x_j} (\rho \bar{u}_i \bar{u}_j) = \frac{\partial}{\partial x_j} \left( \mu \frac{\partial \sigma_{ij}}{\partial x_j} \right) - \frac{\partial \bar{P}}{\partial x_i} - \frac{\partial \tau_{ij}}{\partial x_j} \quad (6)$$

where  $\sigma_{ij}$ , and  $\tau_{ij}$  are given by:

$$\sigma_{ij} = \left[ \mu \left( \frac{\partial \bar{u}_i}{\partial x_j} + \frac{\partial \bar{u}_j}{\partial x_i} \right) \right] - \frac{2}{3} \mu \frac{\partial \bar{u}_i}{\partial x_i} \delta_{ij} \quad (7)$$

$$\tau_{ij} = \rho \bar{u}_i \bar{u}_j - \rho \overline{u_i u_j} \quad (8)$$

$$\tau_{ij} - \frac{1}{3} \tau_{kk} \delta_{ij} = -2 \mu_t \bar{S}_{ij} \quad (9)$$

where  $\bar{S}_{ij}$  is the rate of strain tensor and  $\delta_{ij}$  is the Kronecker delta. We employ the Smagorinsky–Lilly subgrid model (Smagorinsky, 1963; Lilly, 1992) given by:

$$\mu_t = \rho L_s^2 |\bar{S}_{ij}| \quad (10)$$

where  $L_s$  is the mixing length.

### 3. Measurement data

We evaluated our simulations against the data collected from Near Roadway Tracer Study (NRTS08), which was conducted near the Idaho National Laboratory (INL) by the Air Resources Laboratory (ARL) of the National Oceanic Atmospheric Administration (NOAA) and in collaboration with the Atmospheric Modeling and Analysis Division of the U.S. Environmental Protection Agency (EPA). A detailed description of the experiment can be found in Finn et al. (2010). A brief summary is presented here. The experiment was performed in order to characterize the effect of a solid barrier on tracer gas concentration under a variety of atmospheric stability conditions. In the experiment, a solid barrier 6 m high by 90 m long was erected from straw bales in an open field near the INL in order to approximate a typical solid sound barrier found near many highways. Tracer gas, Sulfur Hexafluoride (SF<sub>6</sub>), was released from a 54 m line source located 6 m upwind of the barrier. This gas was chosen due to negligible background concentrations. An array of bag samplers, depicted in Fig. 1, was used to measure the spatial

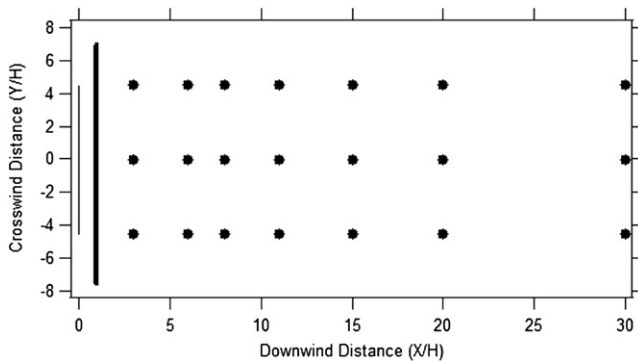


Fig. 1. Schematic showing measurement points for the barrier site in NRTS08. The clearing site has the same configuration except the presence of the barrier. Solid barrier is bold line. The thin line represents the line source. Samplers are represented by dots.

gradients of SF<sub>6</sub> concentration behind the barrier at various downwind and crosswind locations and in an identical configuration in a nearby clearing (i.e., without a barrier). All heights and distances have been normalized by the barrier height, i.e.  $H = 6$  m. Anemometers were placed  $6H$  downwind of the tracer release point at vertical heights of  $.5H$ ,  $1H$ , and  $1.5H$  and  $11H$  downwind of the tracer release point at a height of  $.5H$  in order to characterize the aerodynamic effect of the barrier. A meteorological tower with 1 Hz anemometers at 3 m and 30 m vertically was used to characterize the approach flow of the atmospheric boundary layer including wind speed, wind direction, turbulence characteristics, friction velocity, and atmospheric stability. Additionally, a nearby mesonet tower measured wind speed at 10 m height. All recorded measurements are conservatively considered accurate to within 20%, and usually accurate within 10%.

### 4. Geometry, mesh and boundary conditions

A geometry representing the experimental site was created and meshed in ANSYS Gambit. Separate domains were created for the clearing site and the barrier site. Each domain has dimensions of 300 m long, 180 m wide and 100 m high. The barrier is placed 30 m from the inlet of the domain and the domain extends 90 m past the location of the final sampling point to ensure there is no interference from the boundaries of the domain outlet on the measurement comparison (Cowan et al., 1997). A small emissions zone was created measuring 54 m long by .25 m wide and .25 m high centered 1 m above ground level placed 6 m upwind of the barrier. A structured mesh consisting of 4,178,431 elements for the barrier case and 561,600 elements for the no barrier case was created. The high number of elements in the barrier case is a result of the need to create a finer mesh in the region near the barrier. A mesh refinement test showed this level of refinement to be necessary to accurately resolve the LES model. A coarse mesh containing approximately one eighth the number of elements for both the barrier and no barrier cases and a more refined mesh containing approximately four times the number of elements were created. The RANS model showed virtually no difference in velocity or concentration results between the three meshes for either the barrier or no barrier cases. For the LES model, the difference between the coarse and nominal meshes for any of the velocity or concentration results was no more than 6%. The more refined mesh showed only slight differences with the nominal mesh, showing at most a 2% difference. It is assumed that the huge computational increase from the more refined mesh is too great for the marginal benefit in accuracy.

In addition to the geometry, boundary conditions are required in order to perform the simulation. The ground and barrier are considered to be a no-slip wall. The inlet of the domain is set to be a velocity inlet, where profiles of wind speed, TKE and turbulent dissipation must be provided. The outlet is assumed to be a simple outflow condition. The top of the domain, assumed to be sufficiently far away from the barrier as to not affect the flow in the area, is set to a no-shear condition. The sides of the domain are set to periodic boundary conditions.

Careful attention is needed at the inlet of the domain as inlet flow conditions will greatly affect the simulation results. The meteorological tower measurements of wind speed at 3 m and 30 m height were used to generate the inlet velocity profile. Since two measurement points at different heights were available, the standard power law atmospheric boundary layer profile, given by Equation (11), was used to fit the data.

$$U(z) = U_{\text{ref}} \left( z/z_{\text{ref}} \right)^p \quad (11)$$

**Table 1**  
Inlet flow velocity, turbulence and atmospheric stability for stable, neutral and unstable scenarios.

Atmospheric stability	$u$ ( $z = 3$ m) ( $m s^{-1}$ )	$u$ ( $z = 30$ m) ( $m s^{-1}$ )	Direction (degrees)	TKE ( $m^2 s^{-2}$ )	$u^*$ ( $m s^{-1}$ )	$z/L$	Duration (min)
Stable	3.61	8.71	8.1	.3224	.3110	.048	90
Neutral	7.44	10.75	14.3	1.2503	.8087	-.015	60
Unstable	1.65	2.14	-28.1	.1056	.2925	-.312	45

where  $U_{ref}$  is the velocity at reference height  $z_{ref}$  and  $p$  is an empirically determined coefficient which increases with increasing surface roughness and increasing atmospheric stability (Huang, 1979).

Since this is a two-parameter model, the model is fully constrained by the tower measurements. The 10 m mesonet tower was used to validate the use of the power law profile by comparing the experimental measurement with predicted 10 m velocity from model. The error was found to be 5.00%, 4.54%, and 4.76% for the stable, neutral, and unstable cases, respectively, which indicate that we were able to capture the inlet velocity profiles with good accuracy.

Additionally, turbulence characteristics must be specified at the inlet to the domain. For the steady  $k-\epsilon$  model, this included TKE and turbulent dissipation. TKE was determined from the filtered velocity data according to the equation:

$$TKE = \frac{1}{2} (u'^2 + v'^2 + w'^2), \tag{12}$$

where  $u'$ ,  $v'$  and  $w'$  are the fluctuating components of the velocity in the  $x$ ,  $y$ , and  $z$  directions, respectively. Turbulent dissipation was characterized by the equation:

$$\epsilon = zu_*^3 / \kappa, \tag{13}$$

where  $u_*$  is the friction velocity and  $\kappa$  is the Von Karman constant equal to .41. For the unsteady LES simulation, instantaneous velocity fields must be generated at the domain inlet. A vortex method based on the Spectral Synthesizer method is used (Kraichnan, 1970; Smirnov et al., 2001). The method produces

a perturbation to the mean velocity at each grid point and time step based on the inlet TKE and turbulent dissipation.

### 5. Modeling scenarios

For this study, we consider several representative subsets of the experimental data. The subsets of data were selected based on the criteria of statistically steady flow properties and various atmospheric stability, as discussed below. We are interested in a validating the model under a variety of atmospheric stability classes. The applicability of various flow models to represent various atmospheric stability conditions is an active topic of research (Hargreaves and Wright, 2007; Pontiggia et al., 2009). For this work, we are careful to select periods of data that exhibit strongly steady conditions to minimize any potential issues with varying atmospheric conditions.

An important parameter in characterizing atmospheric stability is the Monin–Obukhov Length (Obukhov, 1971), which is interpreted, physically, as the height at which the production of turbulence from both buoyancy and wind shear is equal and is given by the equation:

$$L = \frac{-u_*^3 \rho c_p T}{\kappa g q} \tag{14}$$

where  $c_p$  is the specific heat of air,  $T$  is absolute temperature,  $g$  is gravitational acceleration and  $q$  is vertical heat flux at the surface. Typically, atmospheric stability is presented as the ratio  $z/L$ , which non-dimensionalizes vertical height by the Monin–Obukhov Length. Finn et al. (2010) computed the atmospheric stability

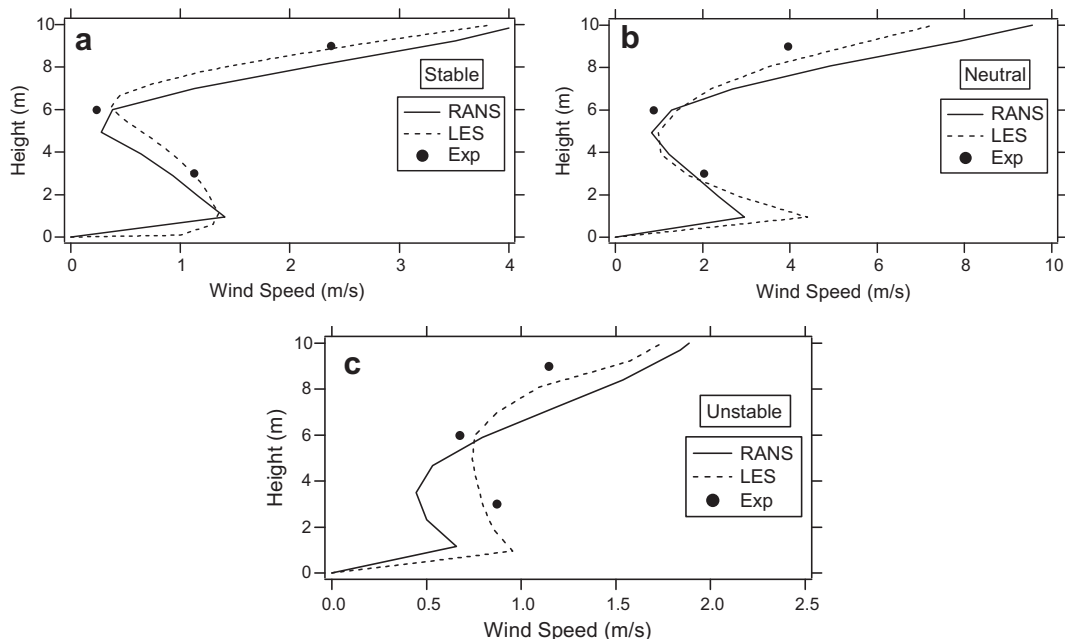


**Fig. 2.** Vertical velocity profiles 4H downwind for scenarios: a) stable, b) neutral, and c) unstable.

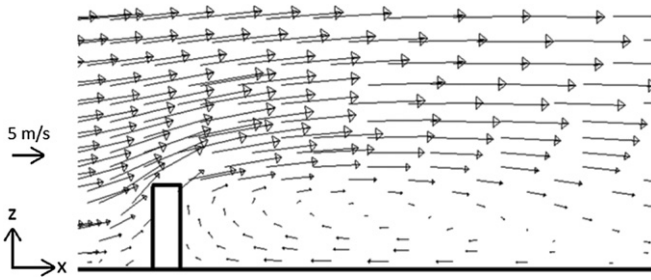


Fig. 3. Illustration of flow recirculation shown by velocity vectors of side view along plume center plane perpendicular to the barrier. Aspect ratio is 1:1.

parameter,  $z/L$ , for each dataset, calculated from the turbulence measurements at the no barrier site, upwind of the tracer release line, and presented scenarios representing stable, neutrally stable, and unstable conditions. Generally speaking, a neutrally stable atmosphere corresponds to a stability parameter of zero, while

more positive and negative  $z/L$  values correspond to more stable and unstable conditions, respectively.

For our study, a subset of data from each of these three scenarios was selected for simulation and comparison. The data subsets will be selected on the basis of statistically steady wind speed, i.e. the mean wind speed does not fluctuate, even though the instantaneous wind speed does. This selection criterion will allow for a more appropriate comparison between the models. Since we only use the RANS model to simulate steady flow conditions and the LES model is necessarily unsteady, we can use the statistically steady experimental data and compare it to both the RANS results and an ensemble average of the LES results. In order to characterize statistical steadiness, the anemometer data was filtered using a simple first-order low pass filter. The high frequency data was used to determine turbulence characteristics and the low frequency data is assumed to be the mean wind flow. We considered only time periods where the mean flow maximum and minimum differ by less than 5%. While the anemometer data was collected at 1 Hz, the

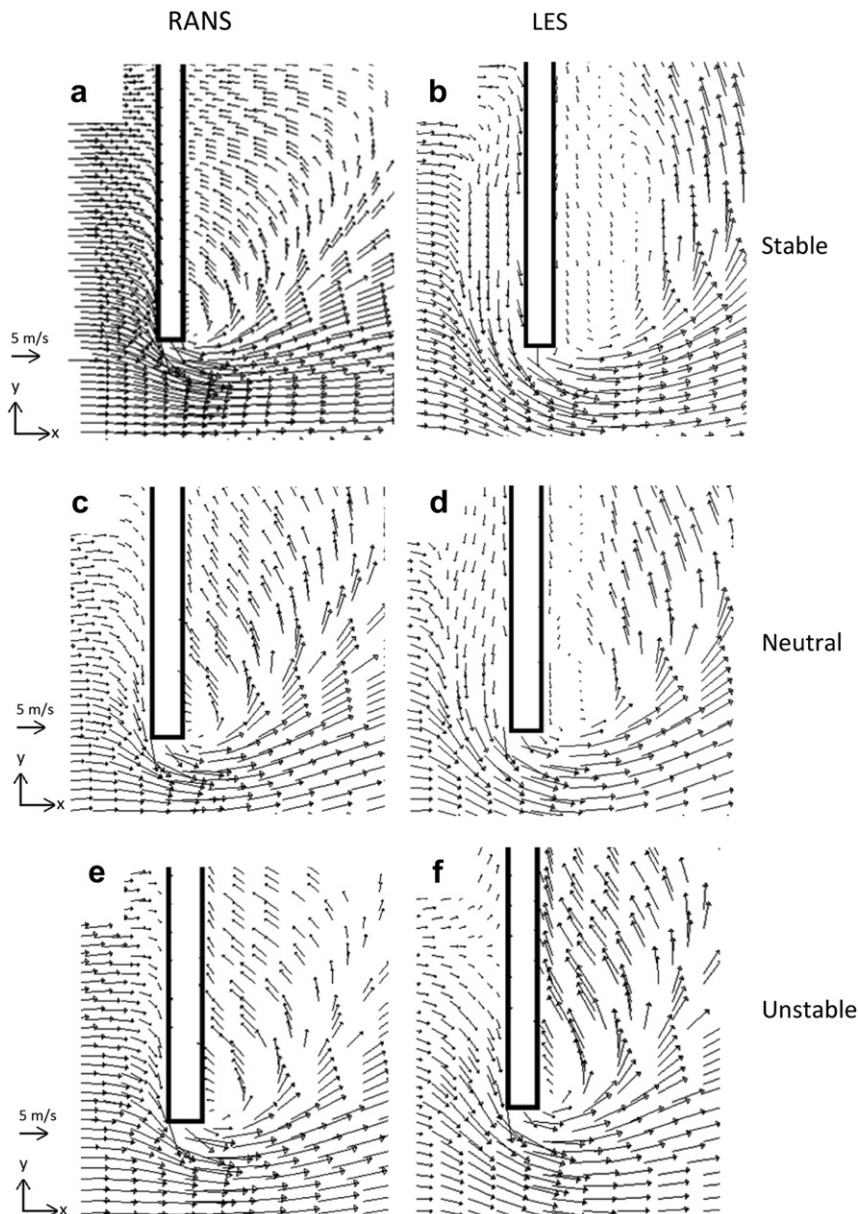


Fig. 4. Velocity vectors for overhead view, at vertical height of 3 m, near  $y/H = -4.5$  (Fig. 1) showing the leading 50 m of the 500 m barrier for different atmospheric stability conditions a) stable RANS, b) stable LES, c) neutral RANS, d) neutral LES, e) unstable RANS, f) unstable LES. Aspect ratio is 1:1.

**Table 2**

Mean fractional error (MFE) between simulation and experiment behind the barrier for vertical velocity at  $x/H = 4$  for stable, neutral and unstable scenarios.

Atmospheric stability	RANS	LES
Stable	.248	.136
Neutral	.261	.225
Unstable	.248	.102

**Table 3**

Mean Fractional Error (MFE) between experiment and the RANS and LES models behind the barrier and in the clearing for SF<sub>6</sub> concentration for stable, neutral and unstable cases.

Atmospheric stability	Location	No barrier RANS	No barrier LES	Barrier RANS	Barrier LES
Stable	−4.5H	.353	.349	.251	.177
	0H	.033	.064	.105	.088
	4.5H	.038	.054	.091	.059
Neutral	−4.5H	.101	.091	.645	.175
	0H	.099	.086	.137	.092
	4.5H	.237	.214	.251	.221
Unstable	−4.5H	.073	.090	.717	.107
	0H	.118	.097	.155	.133
	4.5H	.214	.198	.093	.135

SF<sub>6</sub> bag samplers only report 15-min mean concentrations. Therefore, to ensure we have applicable concentration data, only subsets of wind velocity data which begin and end at 15 min intervals are considered. We selected the longest continuous subsets of data which conform to the above conditions. The total measurement time for the scenarios representing stable, neutral, and unstable atmospheric stabilities were found to be 90, 60, and 45 min, respectively. Table 1 shows the measured velocity for each of the modeled time periods as well as wind direction as measured from perpendicular to the barrier, turbulent kinetic energy, friction velocity ( $u^*$ ) and atmospheric stability parameter ( $z/L$ ) and the duration of the sample period.

**6. Results and discussion**

Simulation results were obtained for the three atmospheric stability conditions for both the barrier and no barrier cases for both the RANS and LES models. Additionally, we performed a sensitivity analysis to characterize the effects of wind speed and direction on pollutant transport.

**6.1. Velocity results**

Fig. 2 shows the vertical velocities behind the barrier for each case comparing the  $k-\epsilon$  and LES to experimental measurements. Flow around a barrier is often highly complex. Recirculation zones, formed in the wake of the barrier and characterized by strong mixing, are regions where a flow vortex attaches to the downwind side of the barrier as seen by the vector plot given in Fig. 3. Additionally, the flow moving around the edge of the barrier can be observed to deflect inward towards the barrier, sometimes causing secondary recirculation. These edge effects can be observed in Fig. 4, which shows the flow around the leading edge of the barrier.

From Fig. 2 it is clear that both RANS and LES perform generally well at capturing the general shape of the recirculation zone behind the barrier. Table 2 tabulates mean fractional error (MFE) for these velocity results. MFE is a statistic used to capture the overall difference between two sets of data given by the equation:

$$MFE = \frac{1}{N} \sum_1^N \frac{C_{1,i} - C_{2,i}}{(C_{1,i} + C_{2,i})/2} \tag{15}$$

where  $N$  is the total number of comparison points and  $C_1$  and  $C_2$  are the two sets of data to be compared (Table 3).

The LES MFE is lower in all three scenarios, indicating the superiority of the LES model in capturing recirculating flow. It should be noted that some of the errors that seem high at around 25% MFE can be attributed to the sharp velocity gradients around the measurement points.

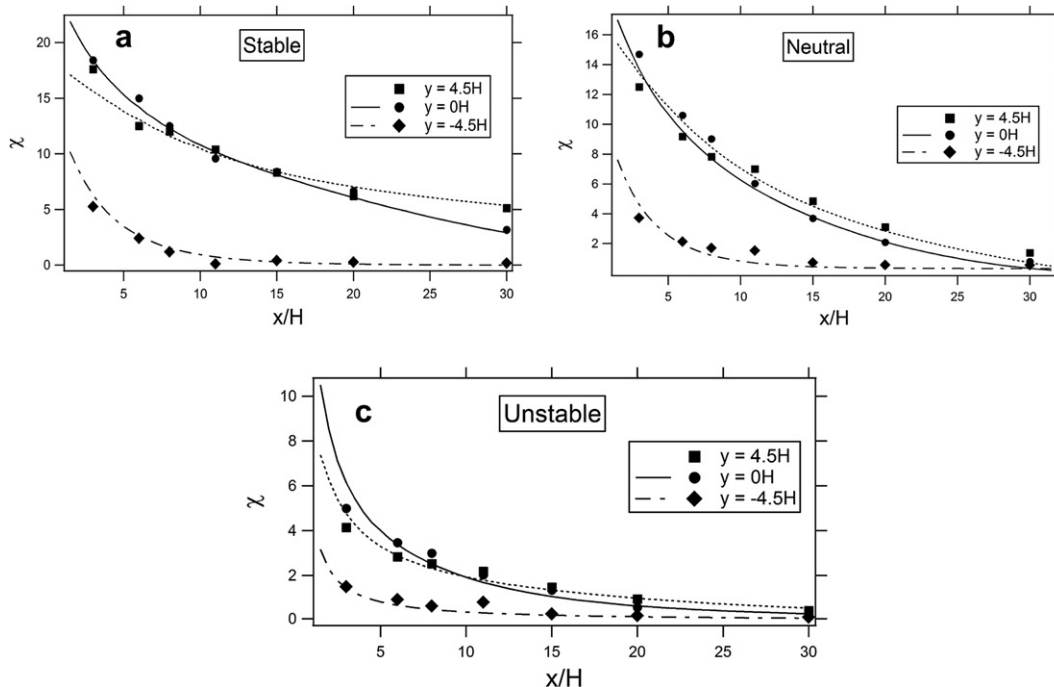


**Fig. 5.** Normalized tracer concentration,  $\chi$ , given by Equation (15), for clearing sites comparing experiment (markers) to RANS model (lines), for scenarios: a) stable, b) neutral, and c) unstable. LES results not included due to close similarity to RANS results.

Experimental data for wind speed is available only along the center of the barrier. However, it is also beneficial to compare how the two turbulence models behave in the region near the leading edge of the flow, where secondary recirculation due to edge effects occurs. The vector plots in Fig. 4 show the comparison of the two models. There are two distinct differences between the models common to all three scenarios we can observe. First, the flow upwind of the barrier is observed to deflect in the negative  $y$  direction a greater distance before the barrier for the LES model as compared with the RANS model. Second, the flow around the edge turns back towards the barrier more sharply for the RANS model. It should be noted that these differences are larger for the stable and neutral cases than the unstable case. This is likely due to the lower wind speed in the unstable case causing less overall flow recirculation.

## 6.2. Tracer concentration results

### 6.2.1. No barrier cases

Fig. 5 shows the tracer results in the clearing along several lines of constant crosswind distance according to Fig. 1 comparing the

experimental data to the RANS model. Results were obtained at crosswind distances of  $+4.5H$ ,  $0H$ , and  $-4.5H$ . Concentration,  $c$ , has been normalized similarly to Finn et al. (2010), by:

$$\chi = \frac{\rho c u_r L_x L_y}{Q} \quad (16)$$

where  $\rho$  is the tracer density,  $u_r$  is the reference wind speed at the clearing at 3 m height,  $L_x$  is the length of the line source,  $L_y$  is the virtual roadway length, and  $Q$  is the release rate.

The results for the LES model are not included in the figure due to the very close similarity to the RANS results. For most points, the difference between the RANS and LES models is less than 5%, only becoming larger than that, but no larger than 10%, in the unstable case past  $x/H = 20$ . The results from the clearing site show a large degree of accuracy between both models and the experiment for each of the atmospheric stability classes, as seen by the mean fractional error (MFE) results in Table 3. There are 3 cases where the RANS model performs better than the LES model, but all of these cases occur when both models produce MFE values less than .1. Therefore both models still perform well and the fact that the RANS model performs slightly

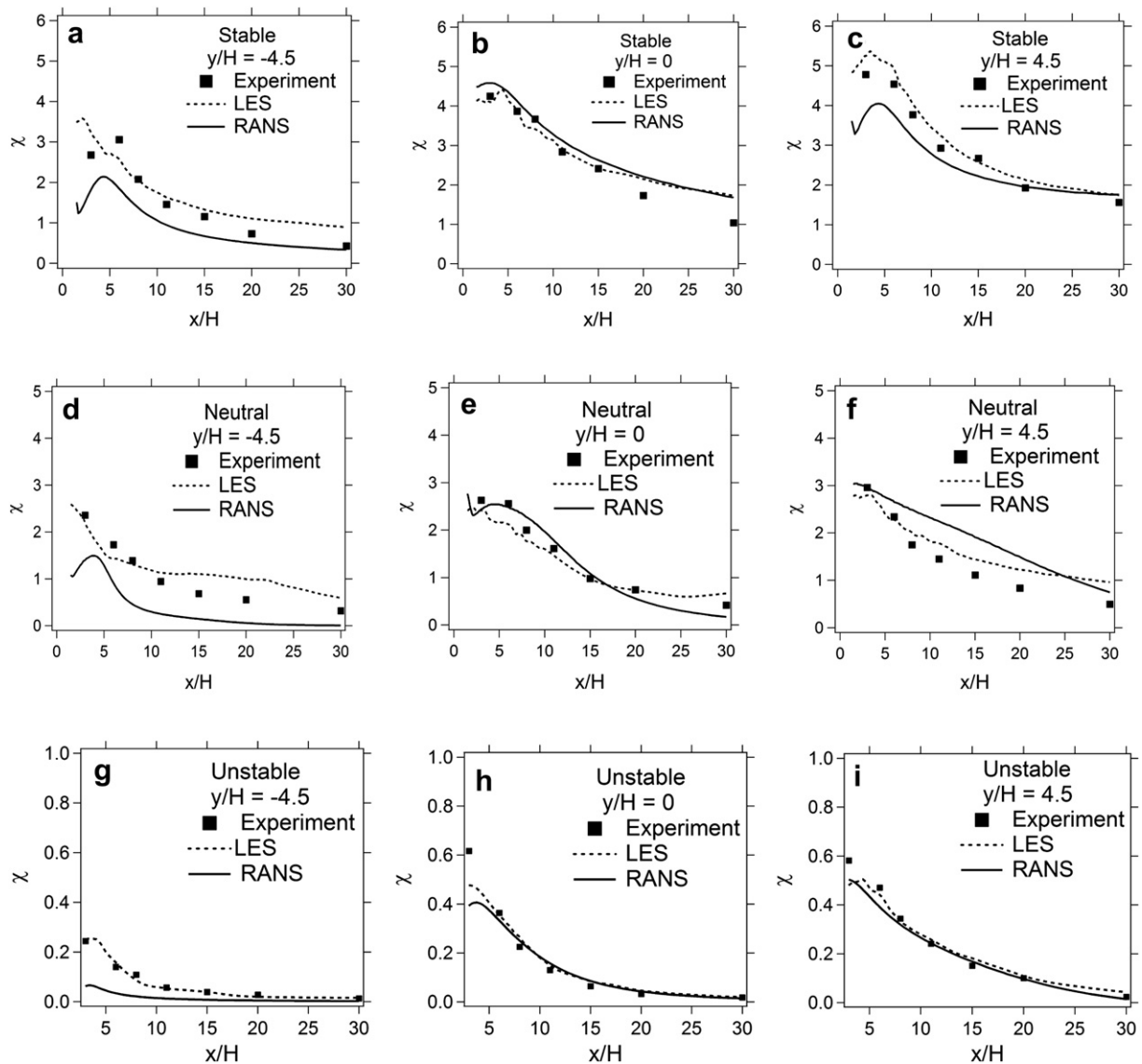


Fig. 6. Profiles of normalized tracer concentration,  $\chi$ , given by Equation (15) comparing experimental data to RANS and LES models for a) stable  $y/H = -4.5$ , b) stable  $y/H = 0$ , c) stable  $y/H = 4.5$ , d) neutral  $y/H = -4.5$ , e) neutral  $y/H = 0$ , f) neutral  $y/H = 4.5$ , g) unstable  $y/H = -4.5$ , h) unstable  $y/H = 0$ , i) unstable  $y/H = 4.5$ .

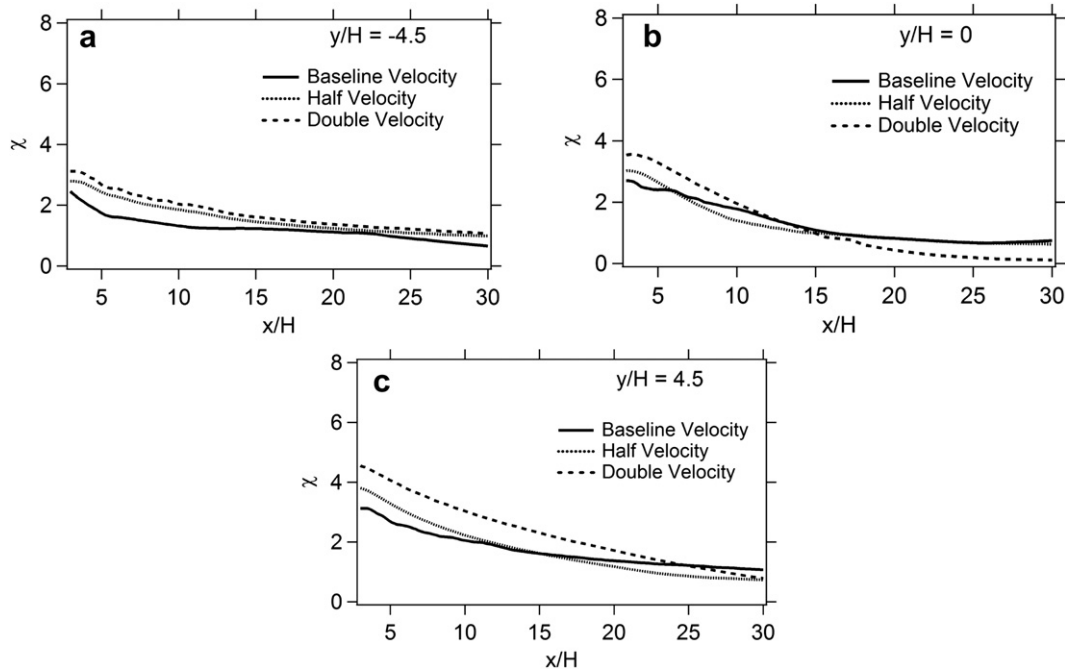


Fig. 7. Normalized downwind concentration,  $\chi$ , given by Equation (15), sensitivity to wind speed for a)  $y/H = -4.5$ , b)  $y/H = 0$ , and c)  $y/H = 4.5$ .

better is inconsequential. Likely, the lack of any disturbances in the flow field from the barrier reduces the complexity of the flow. For these cases, a lower accuracy turbulence model, such as RANS, is sufficient to capture the flow fields without a barrier.

6.2.2. Barrier cases

The presence of the barrier creates a much more complex flow field. Fig. 6 shows the concentration results for each of the stability cases for both RANS and LES at crosswind locations of  $4.5H$ ,  $0H$ , and  $-4.5H$ . It is clear that the LES model performs generally better than the RANS model, as seen by the mean fractional error (MFE) tabulated in Table 3. Additionally, the LES model shows to be highly accurate for almost all scenarios, while the RANS model shows the same level of accuracy for only some of the scenarios. The only scenario where the RANS model performs slightly better than the

LES model is the unstable case at  $y/H = 4.5$ , where the MFE values are .093 and .135 for the RANS and LES models, respectively, indicating that both models perform very well for this particular case. The regions where LES performs significantly better than RANS are at  $y/H = -4.5$  for each scenario, which is near the leading edge of the flow. This corresponds to Fig. 4, where the largest discrepancies between the RANS and LES flow fields are observed and described in Section 6.1. Likely, LES is needed to better resolve the complex flow phenomena that occur there.

Overall, it is found that the LES model performs better than the RANS model for most cases for both velocity and concentration measurements. The region where the two models differed the most in velocity, i.e.  $y/H = -4.5$ , they also differed the most in concentration. This is reasonable since velocity is a large driver of tracer gas transport.

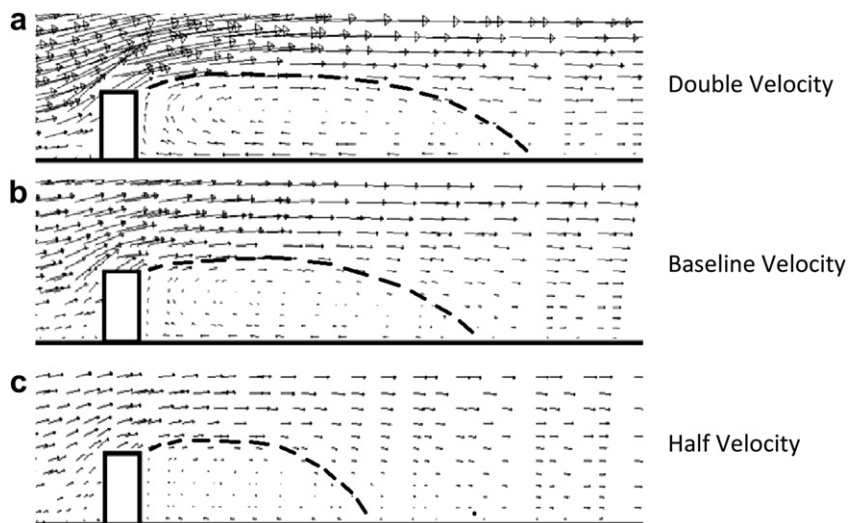


Fig. 8. Velocity vectors along plume center for wind speed sensitivity, showing domain extending  $6H$  downwind of barrier. Recirculation zone demarcated with dashed line. Scenarios a) double velocity, b) baseline velocity, and c) half velocity. Aspect ratio is 1:1.

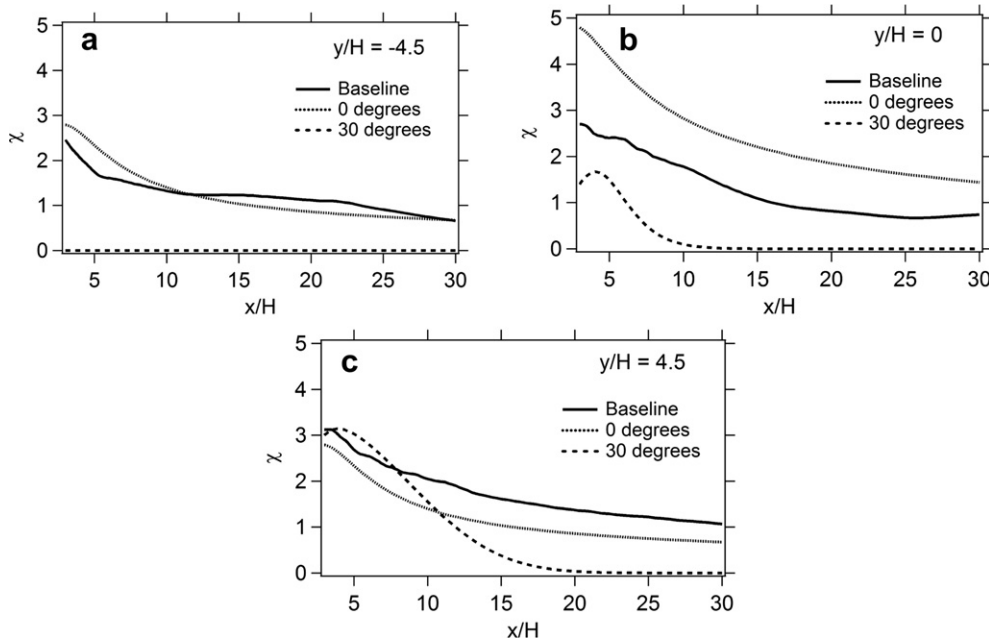


Fig. 9. Normalized downwind concentration,  $\chi$ , given by Equation (15), sensitivity to wind direction for a)  $y/H = -4.5$ , b)  $y/H = 0$ , and c)  $y/H = 4.5$ .

### 6.3. Sensitivity studies

Sensitivity studies were performed to examine how variations in wind speed and wind direction affect concentration results, and particularly observe the effect from the edge and recirculation effects. For these studies, the neutrally stable condition was used as the baseline case. All simulations are performed using the LES model.

To test the effect of wind speed, simulations were performed using an identical inlet wind profile multiplied by a constant value of two or one half. Fig. 7 compares the concentration for the baseline case as well as the double and half wind speed cases. The results show that decreasing wind speed decreases the rate at which tracer can be transported away, thus increasing the tracer concentration. The double velocity case has the opposite effect. For a truly neutral atmospheric stability, we might expect the concentrations to be exactly proportional to wind speed. Thus wind speed should have no effect on  $\chi$ . However, small differences are observed. The discrepancy is likely due to slight deviations from true neutral stability and potential additional effects from the edge of the barrier. Fig. 8 shows the velocity vectors for each of the three cases along the plume center. The general shape of the recirculation zone behind the barrier was found to be the same for each case, but it can be seen in the figure that the faster the wind speed, the larger the recirculation zone. It might be expected that at sufficiently high Reynolds number and neutral stability, the size of the recirculation

zone would be independent of wind speed, further indicating that we may not have truly neutral conditions. Since this region is marked by a large amount of recirculating air, it is expected that there will be more mixing with higher wind speed, thus leading to more gradual decrease in concentration, as observed in Fig. 7. It is also expected that the faster the wind speed, the stronger the edge effects become. Therefore, higher wind speeds are more likely to require a more accurate turbulence model such as LES.

The effect of wind direction is more complex. For the sensitivity analysis, wind angle is measured from the line perpendicular to the barrier, i.e. perpendicular =  $0^\circ$ . We consider three wind angles: the baseline case of  $14^\circ$ , perpendicular to the barrier, and an angle of  $30^\circ$ . Concentration results are shown in Fig. 9. For the perpendicular case, the results at  $y/H = \pm 4.5$  are identical and lower in concentration than those at  $y/H = 0$ , as we expect the flow to be symmetric and disperse horizontally, leading to lower concentrations away from  $y/H = 0$ . For the more oblique  $30^\circ$  case, the concentration at  $+4.5H$  is much greater than the concentration at  $0H$ . The concentration at  $-4.5H$  is insignificant. In the case of the more oblique wind angle, unlike the other cases, the tracer gas does not flow around the leading edge of the barrier. Additionally, the concentrations at  $+4.5H$  and  $0H$  decrease much more rapidly than the other cases as the plume has greater transport in the crosswind direction.

Fig. 10 shows contour plots of the velocity. The greatest crosswind transport is seen for the  $30^\circ$  wind angle, as expected. The figure also shows that the region of low velocity which denotes

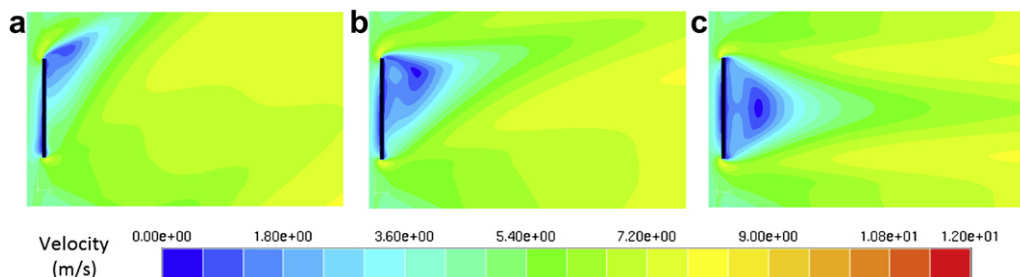


Fig. 10. Velocity contours of entire domain at vertical height 3 m for wind direction sensitivity for a)  $30^\circ$ , b) baseline, and c) perpendicular scenarios. Aspect ratio is 1:1.

a recirculation zone is smaller for the more oblique wind angle and larger for the perpendicular wind angle. Additionally, the edge effects become stronger for more oblique wind angles. Thus, we expect the concentration to reach the background level faster for a more oblique wind angle as the pollutant is transported laterally more quickly. LES is expected to be more appropriate for large wind angles relative to a barrier.

## 7. Conclusions and recommendations

The CTAG model was used to simulate tracer gas concentrations downwind of a solid barrier and in a nearby clearing. Both a RANS model and a LES model were used to simulate the turbulent flow fields and SF<sub>6</sub> dispersion and compared with the NRTS08 dataset. Flow around a solid barrier creates a recirculation zone characterized by an attached vortex downwind of the barrier. It was found that both models are able to capture the general shape of the recirculation zone and velocity and concentration trends. However, for most cases, the LES model was shown to be more accurate overall and to be consistently accurate across all scenarios. In particular, the LES performed better in regions of strong edge effects and recirculation found along the leading edge of the barrier. In these regions of complex flow phenomenon, a more accurate turbulence solver is required.

Due to the high computational cost of the LES model, however, it is helpful to consider the circumstances under which a more simplistic RANS model is sufficiently accurate. Since the greatest inaccuracies appear to stem from edge effects, and these edge effects were found to be stronger during periods of more oblique wind angle or faster wind speeds, a RANS model becomes more applicable the slower and more perpendicular the flow is to the barrier.

Compared with a no barrier scenario, a barrier generally reduces downwind concentration. The amount of reduction is dependent on several factors such as wind speed, direction and atmospheric stability. As such, it is important to understand how these parameters affect concentration. These effects could be deduced with sufficient experimentation, but that is prohibitively expensive. With the CTAG model utilizing a LES turbulence model as described in this paper validated by experiment, however, a wide variety of numerical experiments can be performed to test various parametric effects. Ultimately, these simulations will prove useful in creating a parametric model which can be used to quickly and accurately inform roadway design communities of potential benefits of roadway barrier construction.

## Acknowledgments

We would like to thank Dennis Finn of the National Oceanic and Atmospheric Administration for sharing experimental data. The United States Environmental Protection Agency through its Office of Research and Development funded and managed the research of DKH and SGP described here. It has been subjected to Agency's administrative review and approved for publication.

## References

ANSYS, 2009. ANSYS FLUENT 12.0 Theory Guide. ANSYS, Inc.  
Baldauf, R., Thoma, E., Khlystov, A., Isakov, V., Bowker, G., Long, T., Snow, R., 2008. Impacts of noise barriers on near-road air quality. *Atmospheric Environment* 42, 7502–7507.

Bowker, G.E., Baldauf, R., Isakov, V., Khlystov, A., Petersen, W., 2007. The effects of roadside structures on the transport and dispersion of ultrafine particles from highways. *Atmospheric Environment* 41, 8128–8139.  
Cahill, T., April 2010. How Does Vegetation Affect Pollution Removal. The Workshop on the Role of Vegetation in Mitigation Air Quality Impacts from Traffic Emissions. RTP, North Carolina.  
Chang, C., Meroney, N., 2003. Concentration and flow distributions in urban street canyons: wind tunnel and computational data. *Journal of Wind Engineering and Industrial Aerodynamics* 91, 1141–1154.  
Cowan, I.R., Castro, I.P., Robins, A.G., 1997. Numerical considerations for simulations of flow and dispersion around buildings. *Journal of Wind Engineering and Industrial Aerodynamics* 67, 535–545.  
Finn, D., Clawson, K.L., Carter, R.G., Rich, J.D., Eckman, R.M., Perry, S.G., Isakov, V., Heist, D.K., 2010. Tracer studies to characterize the effects of roadside noise barriers on near-road pollutant dispersion under varying atmospheric stability conditions. *Atmospheric Environment* 44, 204–214.  
Gowardhan, A., Pardyjak, E., Senocak, I., Brown, M., 2011. A CFD-based wind solver for an urban fast response transport and dispersion model. *Environmental Fluid Mechanics* 11, 439–464.  
Hagler, G.S., Tang, W., Freeman, M.I., Heist, D.K., Perry, S.G., Vette, A.F., 2011. Model evaluation of roadside barrier impact on near-road air pollution. *Atmospheric Environment* 45 (15), 2522–2530.  
Hanna, S.R., Tehranian, S., Carissimo, B., 2002. Comparisons of model simulations with observations of mean flow and turbulence within simple obstacle arrays. *Atmospheric Environment* 36, 5067–5079.  
Hargreaves, D.M., Wright, N.G., 2007. On the use of the  $k-\epsilon$  model in commercial CFD software to model the neutral atmospheric boundary layer. *Journal of Wind Engineering and Industrial Aerodynamics* 95, 355–369.  
HEI, 2010. Traffic Related Air Pollution: a Critical Review of the Literature on Emissions, Exposure and Health Effects. HEI Special Report 17. Health Effects Institute, Boston, MA.  
Heist, D.K., Perry, S.G., Brixey, L.A., 2009. A wind tunnel study of the effect of roadway configurations on the dispersion of traffic-related pollution. *Atmospheric Environment* 43, 5101–5111.  
Huang, C.H., 1979. Theory of dispersion in turbulent shear flow. *Atmospheric Environment* 13, 453–463.  
Jones, W.P., Launder, B.E., 1972. Prediction of laminarization with a 2-equation model of turbulence. *International Journal of Heat and Mass Transfer* 15, 301–314.  
Kraichnan, R.H., 1970. Diffusion by a random velocity field. *Physics of Fluids* 13, 22–31.  
Lauder, B.E., Sharma, B.I., 1974. Application of the energy-dissipation model of turbulence to the calculation of flow near a spinning disc. *Letters in Heat and Mass Transfer* 1, 131–138.  
Lilly, D.K., 1992. A proposed modification of the Germano subgrid-scale closure method. *Physics of Fluids A* 4 (3), 633–636.  
Neophytou, M., Gowardhan, A., Brown, M., 2011. An intercomparison of three urban wind models using Oklahoma City Joint Urban 2003 wind field measurements. *Journal of Wind Engineering and Industrial Aerodynamics* 99, 357–368.  
Obukhov, A.M., 1971. Turbulence in an atmosphere with a non-uniform temperature. *Boundary-Layer Meteorology* 2, 7–29.  
Pontiggia, M., Derudi, M., Busini, V., Rota, R., 2009. Hazardous gas dispersion: a CFD model accounting for atmospheric stability classes. *Journal of Hazardous Materials* 171, 739–747.  
Pope, S., 2000. *Turbulent Flows*. Cambridge University Press.  
Smagorinsky, J., 1963. General circulation experiments with the primitive equations. I. The basic experiment. *Monthly Weather Review* 91, 99–164.  
Smirnov, A., Shi, S., Celik, I., 2001. Random flow generation technique for Large Eddy Simulations and particle-dynamics modeling. *Journal of Fluids Engineering – Transactions of the ASME* 123, 359–371.  
Steffens, J.T., Wang, Y.J., Zhang, K.M., 2012. Exploration of effects of a vegetation barrier on particle size distributions in a near-road environment. *Atmospheric Environment* 50, 120–128.  
Tong, Z., Wang, Y., Patel, M., Kinney, P., Chillrud, S., Zhang, K.M., 2012. Modeling spatial variations of black carbon particles in an urban highway-buildings environment. *Environmental Science & Technology* 46, 312–319.  
Wang, Y., Zhang, K.M., 2009. Modeling near-road air quality using a computational fluid dynamics (CFD) model, CFD-VIT-RIT. *Environmental Science & Technology* 43, 7778–7783.  
Wang, Y., Zhang, K.M., 2012. Coupled turbulence and aerosol dynamics modeling of vehicle exhaust plumes using the CTAG model. *Atmospheric Environment* 59, 284–293.  
Wang, Y., McDonald-Buller, E., Denbleyker, A., Allen, D., Zhang, K.M., 2011. Modeling chemical transformation of nitrogen oxides near roadways. *Atmospheric Environment* 45, 43–52.  
Wang, Y., Nguyen, M., Jonathan, S., Tong, Z., Wang, Y.-H., Hopke, P.K., Zhang, K.M., 2013. Modeling multi-scale aerosol dynamics and micro-environmental air quality near a large highway intersection using the CTAG model. *Science of the Total Environment* 443, 375–386.  
Xie, Z., Castro, I.P., 2009. Large eddy simulation for flow and dispersion in urban streets. *Atmospheric Environment* 43, 2174–2185.